Microwave and Hard X-Ray Flare Observations by NoRH/NoRP and RHESSI: Peak-flux Correlations

Säm Krucker[1,2,3] , Satoshi Masuda[1], and Stephen M. White[4]

[1] ISEE, Nagoya University, Japan; krucker@berkeley.edu
[2] Space Sciences Laboratory, University of California, Berkeley, CA 94720-7450, USA
[3] University of Applied Sciences and Arts Northwestern Switzerland, CH-5210 Windisch, Switzerland
[4] Space Vehicles Directorate, Air Force Research Laboratory, Albuquerque NM, USA

Abstract

This paper presents initial results from a statistical study of solar microwave and hard X-ray flares jointly observed over the past two solar cycles by the Nobeyama Radio Polarimeters, the Nobeyama Radio Heliograph, and the Reuven Ramaty High Energy Solar Spectroscopic Imager. As has been previously demonstrated, the microwave (17 GHz and 34 GHz) peak flux shows a linear correlation with the nonthermal hard X-ray bremsstrahlung peak emission seen above 50 keV. The correlation holds for the entire rise phase of each individual burst, while the decay phases tend to show more extended emission at microwaves than is generally attributed to particle trapping. While the correlation is highly significant (coefficient of 0.92) and holds over more than four orders of magnitude, individual flares can be above or below the fitted line by an average factor of about 2. By restricting the flare selection to source morphologies with the radio emission from the top of the flare loop, the correlation tightens significantly, with a correlation coefficient increasing to 0.99 and the scatter reduced to a factor of 1.3. These findings corroborate the assumption that gyrosynchrotron microwave and hard X-ray bremsstrahlung emissions are produced by the same flare-accelerated electron population. The extent of the linear correlation over four orders of magnitude suggests that magnetic field strengths within nonthermal 17 GHz sources are surprisingly similar over a wide range of flare sizes.

Unified Astronomy Thesaurus concepts: Solar x-ray flares (1816)

1. Introduction

Solar flares are believed to be powered by the impulsive release of magnetic energy stored in the solar corona (for a review, see Benz 2017). The release of magnetic energy creates energized particle distributions with strong nonthermal tails in such an efficient and impulsive fashion that they contain a significant fraction of the released energy. In the core of the energy release region, the most efficient flares can create particle distributions where all particles are energized in a bulk process that temporarily creates an essentially nonthermal plasma (e.g., Krucker et al. 2010). Gyrosynchrotron emissions in the microwave range and bremsstrahlung emissions at hard X-ray energies are the two most direct diagnostics of nonthermal flare-accelerated electrons. Gyrosynchrotron has a strong dependence on magnetic field strength, while HXR emission requires ambient density. Radio and hard X-ray diagnostics of flare electrons are thus highly complementary, and combined observations are a key diagnostic tool of solar flare physics (for a review, see, e.g., White et al. 2011).

In the standard scenario, which is essentially unchanged since it was first suggested by Peterson & Winckler (1958), flare-accelerated electrons spiral along coronal magnetic field lines in the corona and radiate incoherent gyrosynchrotron emission. As the density is relatively low in the corona, hard X-ray bremsstrahlung photons are mainly produced after the accelerated electrons propagate to the feet of the field lines and enter the much denser chromosphere. Hence, microwave sources outline coronal magnetic field lines that are occupied by energetic electrons, while hard X-rays tend to show the magnetic connections ("footpoints") of these flaring loops with the chromosphere. This simple picture is somewhat modified by the fact that the intensity of gyrosynchrotron emission is strongly dependent on the magnetic field strength (e.g., Dulk & Marsh 1982). Hence, regions of stronger magnetic fields radiate more strongly than regions of weaker field strength if the nonthermal electron populations are the same. Furthermore, electrons can mirror the converging magnetic field of the legs of flare loops and a "leaky" trap is formed. The trap can limit precipitation and access to stronger-field regions, but trapped electrons produce much more radio emission than precipitating electrons alone simply because trapped electrons stay longer in the corona and therefore have more time to radiate. Because of all of these effects, microwave images may show different source locations in the corona, depending on the magnetic field topology and the actual spatial and energy distribution of accelerated electrons. For some flares, the gyrosynchroton emission is dominated by sources low in the legs of the flare loop (e.g., SOL2002-04-21, Kundu et al. 2004), while in other flares the radio emission is most prominent at the loop top (e.g., SOL1999-05-29, White et al. 2002). Radio source locations are also frequency-dependent, with higher frequencies tending to originate from locations of higher magnetic field strength. Within the same loop structure, higher frequencies are therefore expected from lower altitudes than sources at lower frequencies. Furthermore, the source locations can change in time as the flare evolves (e.g., SOL2002-04-21). We note that this discussion of radio source locations assumes that the radio emission is optically thin, which is usually true at 17 GHz and above: at frequencies below the peak in the radio spectrum, typically around 10 GHz, at least parts of the radio source are optically thick, and the source location then has different properties at different frequencies (e.g., see the model discussion in White et al. 2002).
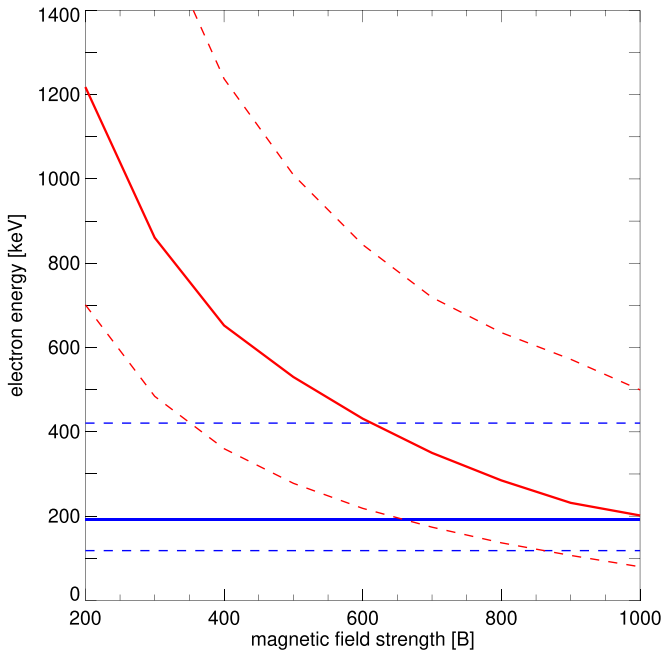
Figure 1. Electron energy ranges contributing to gyrosynchrotron emission at 17 GHz (red lines) and thick-target bremsstrahlung at 100 keV (blue lines). For both curves, a power-law electron spectrum with $\delta = 4$ is assumed (see Bastian 1999 and Kosugi et al. 1988 for details). The solid lines give the main contributing electron energy, while the dashed lines represent the energies above and below the peak with 50% efficiency. For high magnetic field strengths, the hard X-ray- and radio-producing electron ranges are roughly similar, while for weak magnetic fields the hard X-ray emission is produced by lower-energy electrons compared to the radio emissions.

The hard X-ray source structure is also generally more complex than the simplistic picture in which only footpoint sources can be detected. High-sensitivity hard X-ray observations have revealed that coronal bremsstrahlung emissions, although faint, are a general feature of solar flares (for a review, see Krucker et al. 2008). The faint coronal emissions are generally challenging to observe due to dynamic range limitations in current instrumentation. However, partially limb-occulted events that block the bright chromospheric emission reveal that essentially all flares have faint coronal sources (e.g., Krucker & Lin 2008). In a few rare cases, coronal hard X-ray sources can be surprisingly bright (e.g., Masuda et al. 1994), but are more typically below the imaging capability of current-day hard X-ray observations, i.e., at least one order of magnitude fainter than the footpoints.

The time evolution of nonthermal radio and hard X-ray flare fluxes generally show a good agreement in their onset and initial rise, but the radio peak time tends to be slightly delayed relative to HXR, which is generally attributed to the effect of electron trapping in coronal flare loops (e.g., Silva et al. 2000; Kundu et al. 2001). The peak fluxes in radio and hard X-rays show a good correlation over a wide range of flare size (e.g., Kosugi et al. 1988). This indicates that both emissions are produced by the same electron population. To highlight the typical electron energy ranges that produce the gyrosynchrotron and bremsstrahlung emission, we briefly discuss here the contributing energy ranges for a typical power-law solar flare electron population. Figure 1 shows the main energy ranges that contribute to the microwave flux at 17 GHz as a function of magnetic field strength, assuming optically thin emission from a power-law electron energy distribution of slope $\delta = 4$ (see Bastian 1999 for details). The peak energy of the contribution is

shown as a solid red line, and the dashed curves give the energies at which the contribution has decreased to half of the peak value. The energy range contributing to the 17 GHz signal is rather broad, particularly considering that the contributions from outside the dashed lines are significant as well. For large magnetic field strengths, the contributing energy range narrows somewhat and shifts toward lower energies. The blue lines in Figure 1 represent the corresponding energy ranges that contribute to production of 100 keV bremsstrahlung photons for a power-law electron distribution with the same index as used above, assuming the thick target scenario (see Kosugi et al. 1988 for details). Hard X-ray bremsstrahlung is also produced by a broad range of energies, with the main contribution roughly coming from electrons at double the energy of the photon. For magnetic fields around 1 kG, the contributing ranges for 17 GHz and 100 keV emission are similar, while for magnetic field strengths of only a few hundred Gauss, the energy ranges significantly differ. Contributions from different energy ranges will not change the match in the time profiles of the two emissions if they belong to the same power-law energy distribution. However, if they belong to different populations then one might expect to see differing time profiles. This may happen if there is a break in the nonthermal electron energy distribution, i.e., if there are differently evolving power laws at higher and lower energies, with the break occurring between the energies contributing at radio and HXR wavelengths. Observational studies using the spectral indices of the microwave and hard X-ray data to infer the relevant electron energy distributions reveal that the derived electron spectra tend to agree if the comparison is done at energies above a few hundred keV (Trottet et al. 1998), but the hard X-ray spectrum at lower energies may be consistent with an electron power law that is softer than the spectrum derived from radio data (e.g., Silva et al. 2000). This difference is generally attributed to an upward break in the electron spectrum at a few hundred keV (e.g., Asai et al. 2013). The most straightforward explanation for an upward break is the existence of two components that are potentially produced by two different acceleration mechanisms. To produce the close temporal correlation in radio and hard X-rays, these two acceleration mechanisms must then be closely linked. A second explanation is that the difference in spectral break is because radio emission is predominantly produced by the trapped population, while the hard X-ray spectrum is dominated by precipitating electrons (e.g., Minoshima et al. 2008; Kawate et al. 2012).

Two solar-dedicated observatories have provided daily imaging observations of nonthermal electron activity during the past two solar cycles: the Nobeyama Radio Heliograph (NoRH; Nakajima et al. 1995) at radio wavelengths, and the Reuven Ramaty High Energy Solar Spectroscopic Imager (RHESSI; Lin et al. 2002) in hard X-rays. NoRH observes at two microwave frequencies (17 GHz and 34 GHz) at a time cadence of 1 s or better. The synthesized images have a nominal resolution (FWHM) of order 12 and 6 arcsec at 17 and 34 GHz, respectively, and high dynamic ranges (up to 1:1000) can be achieved. In addition, fixed-frequency total flux measurements at seven frequencies are provided by the Nobeyama Radio Polarimeters (NoRP; Nakajima et al. 1985). NoRH typically observes daily in the time range 22:45–06:30 UT, whereas NoRP observes closer to sunrise and sunset. RHESSI was a NASA Small Explorer mission operating from 2002 through 2018, providing imaging spectroscopy in the hard X-ray range

using rotational-modulation collimators (Hurford et al. 2002) at size scales down to 2″ at a moderate imaging dynamic range of typically less than 1:10. White et al. (2011) summarized the results of previous joint NoRH/RHESSI studies, mainly containing single-event analyses from solar cycle 23. To date, no systematic survey of joint NoRH/NoRP and RHESSI data has been published. In this paper, we discuss the peak flux properties of a sample of solar flares well observed in both radio and hard X-rays. More detailed studies using these sets of observations to explore other aspects of particle acceleration in solar flares are planned for publication in the future.

2. Observations

We selected jointly observed NoRH/NoRP and RHESSI flares with a GOES solar flare class of M7 or larger. The choice of M7 is somewhat arbitrary. Just selecting X class flares, on the other hand, would have limited the sample of events too strongly, while including all M class flares would have included many events with photon counting statistics too low for detailed RHESSI imaging at energies that are unambiguously dominated by nonthermal electrons (photons >50 keV). With the slightly longer daily observing window of NoRP compared to NoRH, the number of flares during the RHESSI mission available at both radio and HXR wavelengths is 40 for NoRP, of which 35 have NoRH imaging.
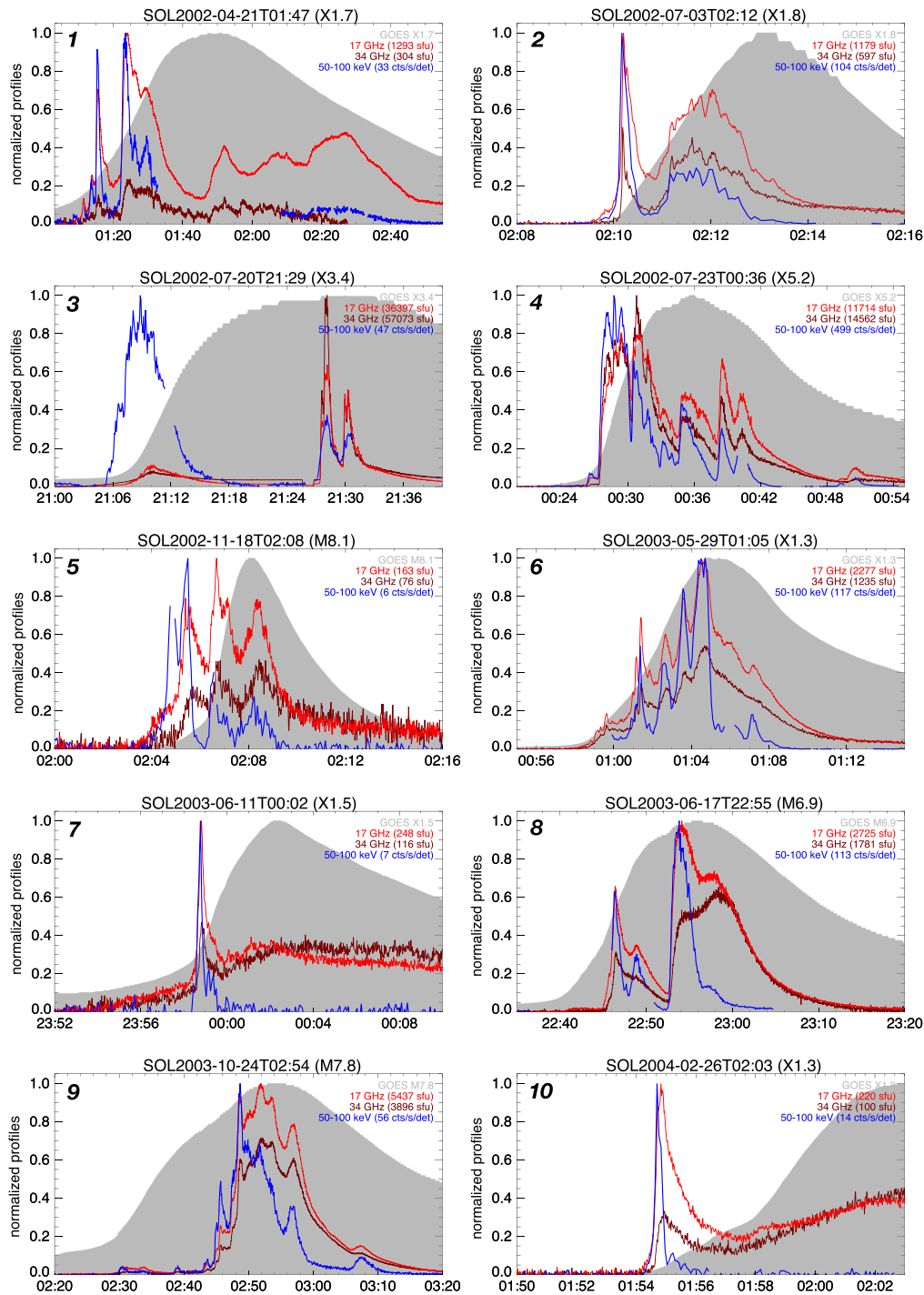
2.1. Time Profiles

As a first step, we discuss here the relative evolution of the microwave and hard X-ray time profiles. For the microwave profiles, we use the standard 1 s cadence calibrated NoRP data products that are available online. For RHESSI, we made use of the standard software to derive light curves from the front segment of the RHESSI detectors (see Smith et al. 2002) at 4 s time cadence. The number of flares with RHESSI rear-segment data which have good statistics is limited (Shih et al. 2009) and they do not add to our statistical study, so we do not include rear-segment data in the analysis. We selected two energy ranges in the hard X-ray range: 50–100 keV and 100–300 keV. The lower limit of 50 keV is used to make sure that the emission is purely nonthermal, without any traces of the thermal component. In addition, it avoids the energy range around ∼30 to ∼40 keV that is most strongly affected by pulse pile up (Smith et al. 2002). The upper energy limit represents the highest-energy photons detected by the front segments.

Figures 2 through 5 provide time profiles for each of the 40 events. The GOES light curve of the low-energy channel (nominally 1–8 Å) is additionally shown as a reference. Our findings match previously reported work well, in that the time profiles in all events show a very clear correlation between the onsets of each individual peak in radio and hard X-rays. This close correlation is especially well seen in SOL2013-10-28 [32] and SOL202-07-23 [4] (see also White et al. 2003); please note that the numbers in brackets following the solar flares correspond to those in the first column of Table 1. The radio light curves tend to show a decay time longer than is seen in hard X-rays, consistent with the expectation that particle trapping in the corona increases the duration of the radio bursts relative to the hard X-ray profiles (e.g., Kundu et al. 2001). This is generally best seen in the later nonthermal bursts within each flare, e.g., SOL2005-09-17 [22] or SOL2013-10-28 [32]. A few bursts show very pronounced signs of trapping, e.g.,

SOL2003-06-17 [8] where the second set of nonthermal bursts occurring around the GOES peak time have much longer durations in radio compared to hard X-rays. In such cases the time profiles at 34 GHz tend to be smooth with less pronounced peaks (e.g., SOL2012-07-19 [28] and SOL2013-05-15 [31]). For most flares the 17 GHz fluxes are above the fluxes detected at 34 GHz. The five strongest radio flares, however, have a peak in the spectrum above 17 GHz (see Table 1), in which case some of the 17 GHz source is likely to be optically thick. It is exceedingly rare for the radio spectral peak to lie above 34 GHz (see, however, Ramaty et al. 1994), so we assume that all the 34 GHz sources in our sample are optically thin.

To quantify these well-established findings in a single plot, we selected all well-defined individual bursts from our set of events and produce a scatter plot showing the paths of the radio and hard X-ray light curves on a radio flux versus hard X-ray count rate plot. Figure 6 (left) shows the results of 82 individual burst components selected from our sample, separated into the rise phase (left panel), defined here as from onset to hard X-ray peak time, and the decay phase (central panel), defined to start after the hard X-ray peak. In the rise phase, the majority of individual bursts show a linear correlation between the radio and hard X-ray flux, and all data points together reveal a correlation over three orders of magnitude, although with a significant scatter. The few events with slightly different slopes are all secondary bursts within flares and therefore may contain not-yet fully decayed radio flux from a previous peak. Such a contribution only happens for the radio fluxes, whereas the hard X-ray bursts generally have fully decayed by the time of the next burst. The decay of each individual nonthermal peak shows a significantly slower decay in radio than in hard X-rays (Figure 6, center). The 4 s time resolution of the RHESSI count rates limits the accuracy of the relative peak times. Nevertheless, the peak of the radio emission is clearly delayed from the hard X-ray peak, with ∼68% having delays at or above 4 s (Figure 6, right panel). This result is in agreement with previous studies (e.g., Silva et al. 2000).

Besides the nonthermal emission, thermal free–free emission may also be seen in the NoRH frequency range, but generally at a lower level than the nonthermal gyrosynchrotron sources (e.g., Morgachev et al. 2014). Optically thin thermal emission scales linearly with emission measure and inversely with the square root of temperature. There is thus a weak preference for colder plasma to contribute more to free–free radio emission. At the temperatures of flare plasma the bremsstrahlung radio emission is almost certainly optically thin at 17 and 34 GHz, in which case thermal flux spectra are constant with frequency, and they are therefore easily spotted in the overview time profiles shown in Figures 2–5 as periods when the 17 GHz and 34 GHz curves lie on top of each other. Clear examples are the late phases of SOL2002-07-03 [2], SOL2002-11-18 [5], SOL2003-06-11 [7], and SOL2004-02-26 [10], where thermal emission with a flat spectrum is seen after the end of the impulsive phase. Typical emission measures and temperatures inferred from the soft X-ray emission of large flares can produce a thermal flux of order 100 sfu, which will be larger if even cooler material not sampled by soft X-rays is also present. During the impulsive peaks the thermal radio emission in these large flares is generally well below the nonthermal contribution, and the peak flux represents the nonthermal emission. For events with rather weak nonthermal bursts, however, the

Figure 2. Overview plot for each of the 40 selected flares with time profiles in UTC at microwaves and hard X-rays as indicated. For reference, the GOES soft X-ray time profile (linear scale) of the low-energy channel (nominally 1–8 Å) is shown in gray. The radio time profiles are normalized to the peak of the value of the stronger of the two frequency channels, while the soft and hard X-ray profiles are normalized separately.

peak flux can have significant contribution from thermal emissions (e.g., SOL2003-06-11 [7] or SOL2011-09-25 [27]). The peak fluxes discussed in the next section have had the thermal contribution removed where necessary.

2.2. Peak Fluxes

In this section, the peak fluxes in the radio, hard X-ray, and soft X-ray domains are compared. We note that while the radio and hard X-ray peaks typically occur within one minute of each other (Figures 2–5), the GOES soft X-ray peak is generally significantly later. For simplicity, only the lower-energy GOES channel (1–8 Å) is used in the correlation plots. On-disk flares and partially occulted flares are distinguished in order to take into account the likelihood that the chromospheric (footpoint) hard X-ray emissions are much more attenuated by partial limb-occultation than the coronal radio emission. Fits to the relationship between the fluxes in the different wavelength ranges are therefore restricted to on-disk events only.

Table 1
Nobeyama/RHESSI Event List

Number	Flare	17 GHz[a]	34 GHz[a]	50 keV[b]	100 keV[b]	Morphology
1	SOL2002-04-21T01:47 (X1.7)	1293	304	33	5.4	leg (17); leg (34)
2	SOL2002-07-03T02:12 (X1.8)	1179	597	104	9.0	unclear
3	SOL2002-07-20T21:29 (X3.4)	36397	57073	47	9.8	only NoRP
4	SOL2002-07-23T00:36 (X5.2)	11714	14562	499	150	top (17); top (34)
5	SOL2002-11-18T02:08 (M8.1)	163	76	5.6	⋯	top (17); top (34)
6	SOL2003-05-29T01:05 (X1.3)	2277	1235	117	24	top (17); top (34)
7	SOL2003-06-11T00:02 (X1.5)	248	116	7.3	⋯	compact
8	SOL2003-06-17T22:55 (M7.0)	2725	1781	113	35	top (17); leg (34)
9	SOL2003-10-24T02:54 (M7.7)	5437	3896	55	18	leg (17); leg (34)
10	SOL2004-02-26T02:03 (X1.3)	221	114	14	⋯	top (17); top (34)
11	SOL2004-07-15T01:41 (X1.9)	692	423	16	2.4	compact
12	SOL2004-07-16T02:06 (X1.4)	1645	1589	144	14	top (17); leg (34)
13	SOL2004-07-22T00:32 (M9.2)	324	166	6.9	⋯	leg (17); leg (34)
14	SOL2004-11-06T00:33 (M9.5)	324	268	21	2.1	top (17); top (34)
15	SOL2004-11-10T02:12 (X2.6)	8435	⋯	403	106	top (17); top (34)
16	SOL2005-01-01T00:31 (X1.8)	4830	2182	232	52	top (17); top (34)
17	SOL2005-01-15T00:43 (X1.3)	4380	3749	143	8.1	top (17); leg (34)
18	SOL2005-01-15T23:03 (X2.7)	12261	⋯	330	88	only NoRP
19	SOL2005-01-20T07:00 (X7.2)	19284	22263	2095	670	only NoRP
20	SOL2005-09-10T22:06 (X2.2)	5897	4564	109	32	only NoRP
21	SOL2005-09-13T23:22 (X1.9)	3017	4757	441	56	compact
22	SOL2005-09-17T06:05 (X1.1)	1972	1340	84	14	top(17); top (34)
23	SOL2006-12-13T02:40 (X3.5)	12609	12895	283	55	leg (17); leg (34)
24	SOL2011-02-15T01:56 (X2.4)	860	444	31	5	unclear
25	SOL2011-03-09T23:23 (X1.6)	292	134	11	⋯	top (17); leg (34)
26	SOL2011-07-30T02:09 (M9.6)	590	283	37	7.2	compact
27	SOL2011-09-25T04:50 (M7.5)	284	154	4.1	⋯	unclear
28	SOL2012-07-19T05:58 (M7.8)	427	209	5	0.9	leg (17); leg (34)
29	SOL2012-10-23T03:17 (X1.8)	2496	4378	419	160	compact
30	SOL2013-05-13T02:16 (X1.8)	2161	1148	25	8	leg (17); leg (34)
31	SOL2013-05-15T01:48 (X1.3)	843	398	23	4.6	top (17); leg (34)
32	SOL2013-10-28T02:03 (X1.1)	2955	1864	53	21	top (17); leg (34)
33	SOL2013-11-10T05:14 (X1.2)	643	469	13	2.5	compact
34	SOL2014-02-25T00:49 (X5.0)	22244	46482	709	347	top (17); top (34)
35	SOL2014-04-25T00:26 (X1.4)	453	188	13	1.5	occulted
36	SOL2014-10-22T01:58 (M8.9)	4152	1368	105	10	top (17); top (34)
37	SOL2014-10-27T00:34 (M7.2)	215	130	0.4	⋯	unclear
38	SOL2015-03-03T01:35 (M8.3)	711	422	5.6	1.5	occulted
39	SOL2015-05-05T22:10 (X2.8)	2343	1526	444	131	only NoRP
40	SOL2016-07-23T05:16 (M7.7)	354	⋯	71	17	unclear

Notes.
[a] Background subtracted peak fluxes in sfu and source location as derived from NoRH.
[b] Background subtracted RHESSI peak count rate in counts per second per detector.

The scatter plot of the peak thermal soft X-rays versus the peak nonthermal radio and hard X-ray fluxes reveals a weak correlation with large scatter (Figure 7). Note that the partially occulted events lie at the bottom of the distribution of hard X-ray fluxes, consistent with a low altitude for the sources, whereas they are more spread out in the distribution of radio fluxes. The dependence of the nonthermal emissions as a function of GOES class is found to increase faster than linear (power-law exponents are between 1.6 and 1.7). This indicates that larger soft X-ray flares are more efficient in electron acceleration, but the scatter from event to event can be very large. We also note here that the GOES class itself is only a measure of a flare's peak soft X-ray output, which cannot be assumed to be linearly proportional to a flare's total released energy. Hence, the interpretation of the fitted power-law coefficient cannot easily be translated into flare size in the sense of released energy. Kawate et al. (2011) has published the 17 GHz versus GOES class correlation without restricting the

range of GOES classes (see Figure 3(a) in Kawate et al. 2011). Although our sample limitation to large flares might be expected to bias our result, both studies find a similar power-law slope of 1.7 for the relationship of 17 GHz and soft X-ray fluxes.

The scatter plots between the two nonthermal quantities show much tighter correlations (Figure 8), with a scatter of roughly a factor of 2 around the fit (we use the term "factor of deviation" for this quantity). There are rather minor differences between the different correlations shown in Figure 8, with the smallest scatter found in the relationship between the 34 GHz and 50–100 keV fluxes (average factor of deviation of 1.8 with a standard deviation of 0.8), and the largest scatter found to be between 17 GHz and 100–300 keV fluxes (2.4 ± 1.6). This is also reflected by the slightly different correlation coefficient as given in the plot. As noted earlier, the fact that some 17 GHz sources are not optically thin may contribute to scatter in the correlation with the optically thin hard X-ray fluxes. More
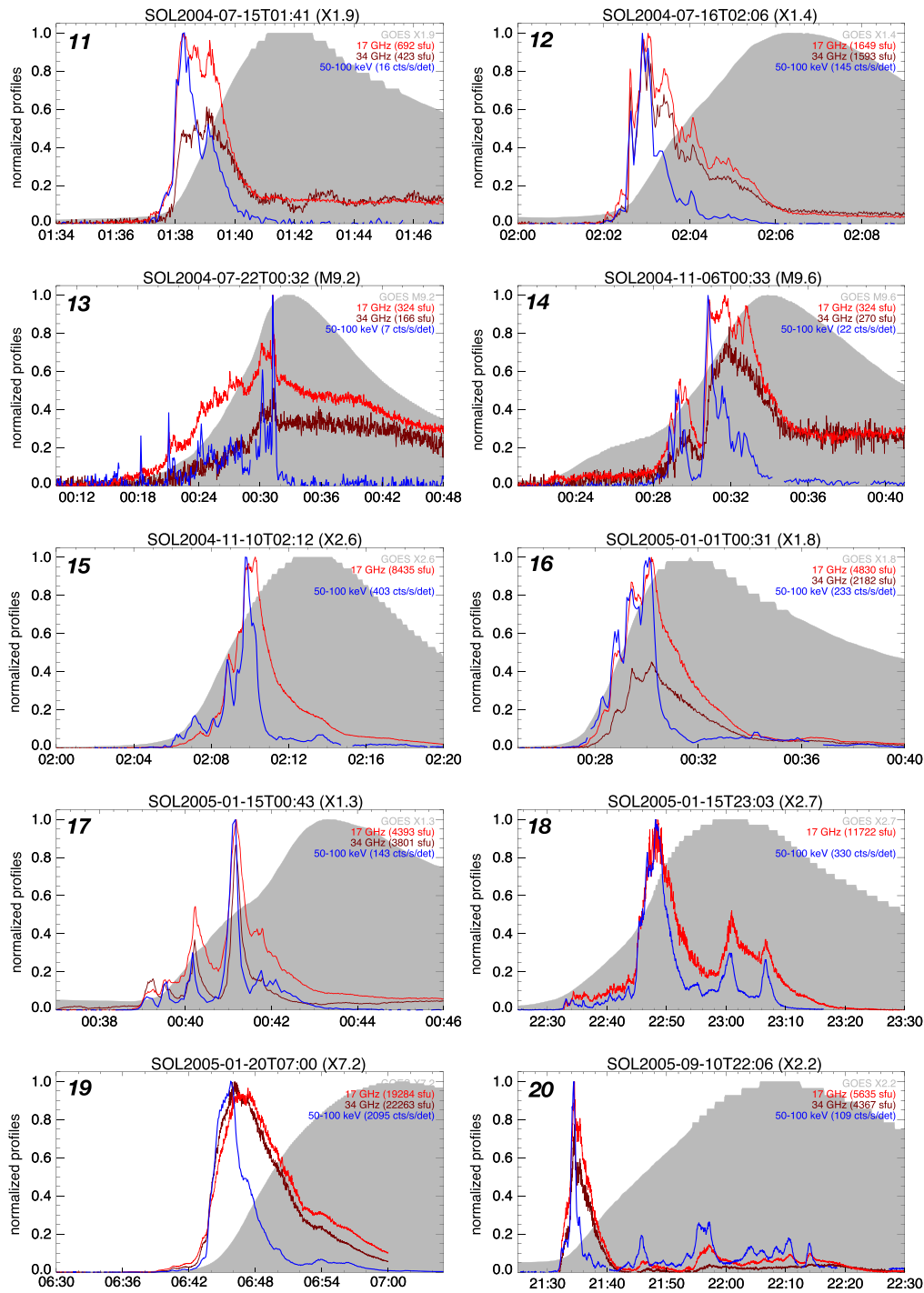
Figure 3. Continuation of flare overview plots.

importantly, the fitted power-law indices are all close to unity, indicating that the two quantities are linearly correlated. The same correlation has been previously reported by Kosugi et al. (1988) in their Figure 1. The much closer correlation between the two nonthermal quantities compared to the correlations with the GOES flux indicates that our use of GOES class as a selection criterion could be missing several strong nonthermal events. To compile a list of all high-quality nonthermal RHESSI/NoRH flares, a better search criteria would have been to select flares above a fixed radio flux or above a fixed

hard X-ray count rate. However, for our statistical study, the selected sample is sufficient.

We searched for trends in the deviations from fits to the whole sample by dividing it into different groups depending on GOES flare class or time delays of the radio peak. However, no additional significant trends are found. The absence of a trend for flares with large time delays in the radio peak indicate that trapping does not significantly increase the radio peak flux, but the main effect is to prolong the decay. We will come back to possible explanations for the deviations in the correlation plot in Section 2.3.
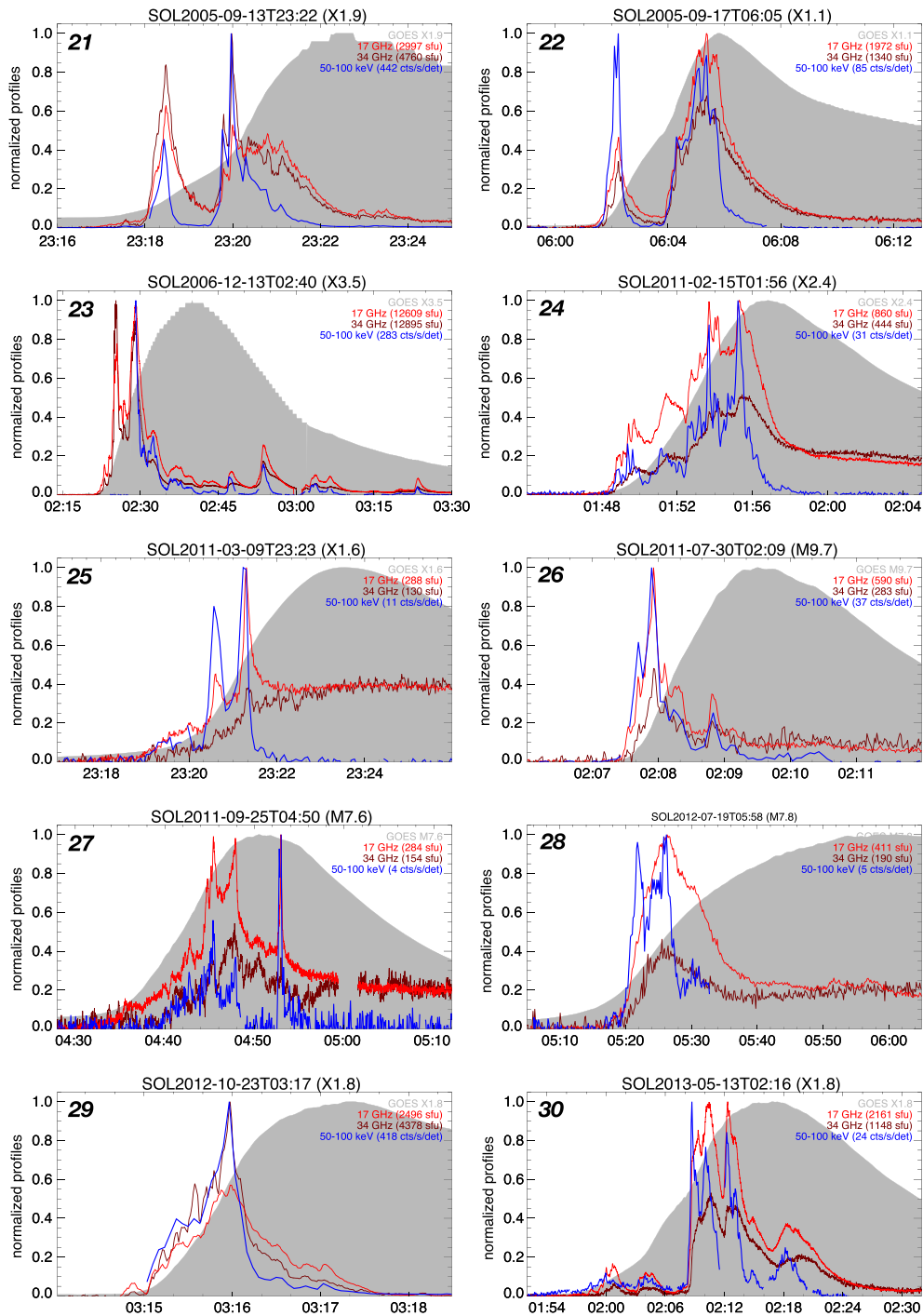
Figure 4. Continuation of flare overview plots.

2.2.1. Peak Fluxes of Smaller NoRP/RHESSI Events

To investigate if the correlation between the nonthermal radio and hard X-ray peak fluxes also holds for smaller flares, we investigated all jointly observed flares during 2002. The choice of this time interval is convenient since it results in a sample with roughly the same number of events as for the main study of our paper, while also limiting the workload. As smaller events are easier to detect at both the lower X-ray energy range and the lower frequency, we limit the investigation to the correlation of the 50–100 keV count rate and the 17 GHz flux. The detection limit for RHESSI events in the 50–100 keV energy range is ∼0.5

counts/s/det, at least for events with low nonsolar background emission. For NoRP, the limit is roughly 10 sfu, depending on daily weather. By chance, these limiting values roughly correspond to the fitted relationship found from the larger-flare correlation in the previous section. Hence, this event sample should not be significantly biased by the different detection sensitivities of the two instruments. We used the existing flare catalogs from RHESSI ("events imaged above 25 keV"; we note here that events imaged by RHESSI in the 25–50 keV range are generally also detected in the 50–100 keV light curves) and NoRH to compile a list of joint events. A few jointly observed events were cut from the list because of a high nonsolar
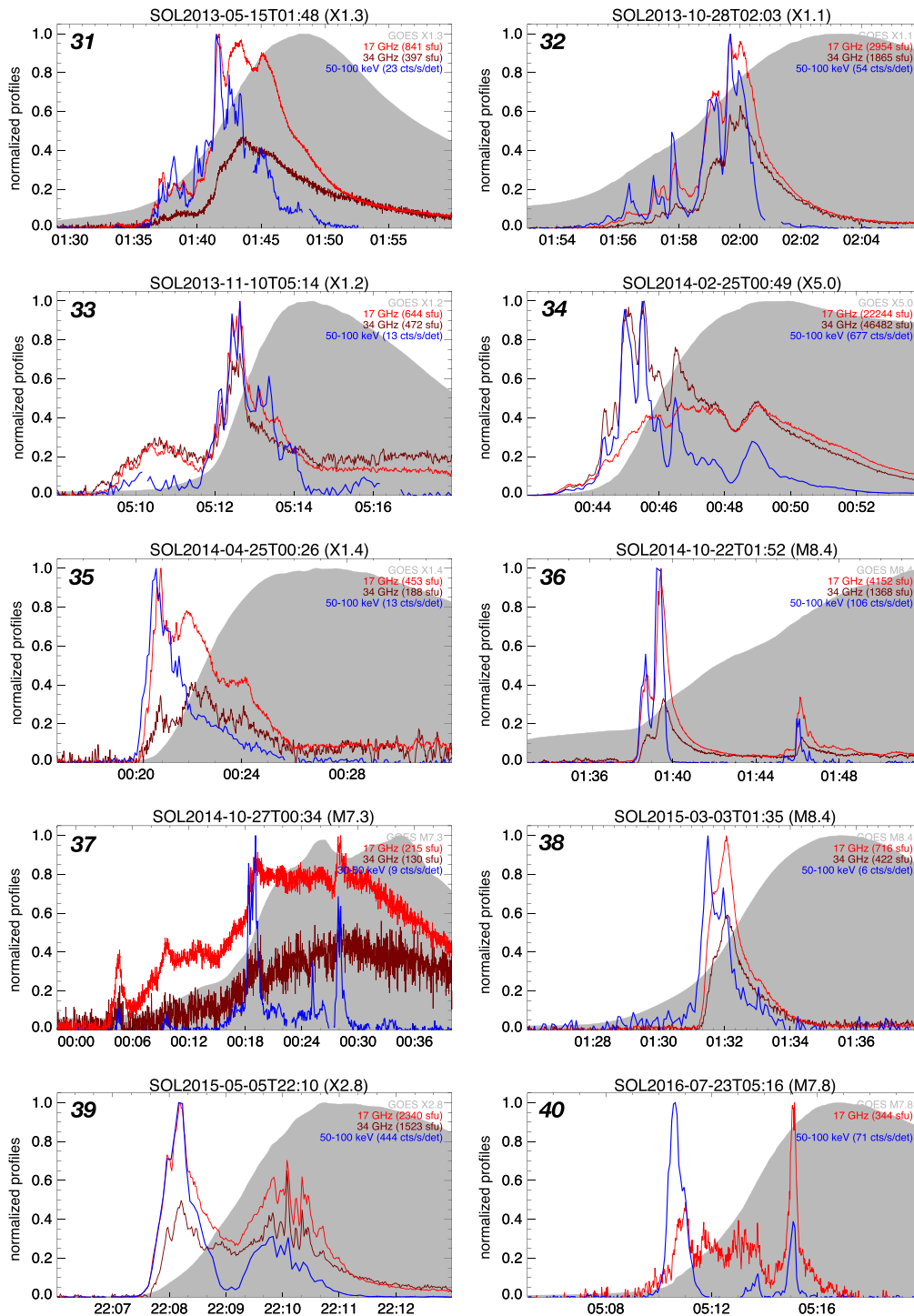
Figure 5. Continuation of flare overview plots.

background in RHESSI, resulting in a total of 36 jointly observed flares in 2002.

The smaller flares from 2002 follow the same trend as seen in the larger flares. Figure 9 shows that correlation between radio and hard X-ray fluxes holds over almost 4 orders of magnitude. The power-law fit to the correlation is consistent with a linear relation with a power-law index of 0.97 ± 0.05. On an individual basis, the deviation of the fit has a scatter of a factor of ~2.2, and 92% of the events are within a factor of 4 of the fitted relationship (Figure 9, top). Out of the 71 total events in the combined (2002 + large flare) sample, there is one outlier, SOL2002-08-12T02, which

shows a steeply decreasing HXR spectrum above 50 keV resulting in a radio-rich event by a factor of 9 relative to the fitted value. We also note that the "intriguing" microflare published by Hannah et al. (2008) with an extraordinarily intense nonthermal component relative to its low GOES class of A2 fits well within the statistical properties found here (see blue data point in Figure 9). Hence, this flare has a "normal" nonthermal component, but a very small thermal component. The other extreme is represented by SOL2002-04-15T23:17UT and SOL2002-10-04T00:47UT, both M1 class flares, with roughly the same nonthermal radio and hard X-ray fluxes as the "intriguing" microflare. Hence, the same
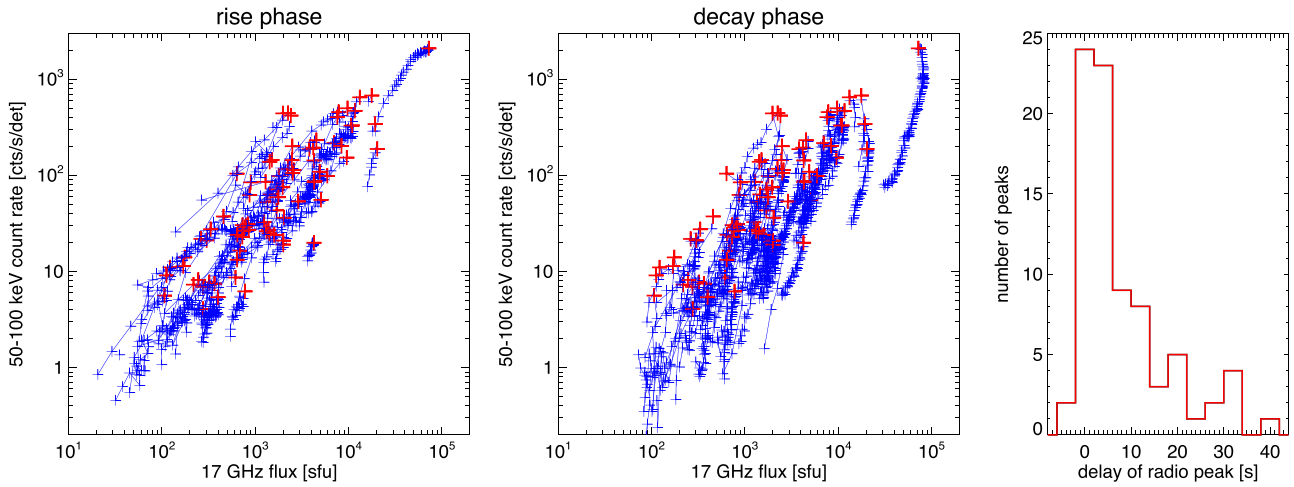
Figure 6. Summary plot of all well-defined individual flare bursts (82 bursts in 40 flares): (left) scatter plot of 17 GHz flux and 50–100 keV count rate from the onset of each burst to the hard X-ray peak, with the hard X-ray peak marked in red. (Center) Same scatter plot but for the decay time after the hard X-ray peak. (Right) Histogram of peak time difference in radio and hard X-rays, with a positive delay corresponding to a later radio peak time, binned at RHESSI's 4 s cadence (the spin period of RHESSI).
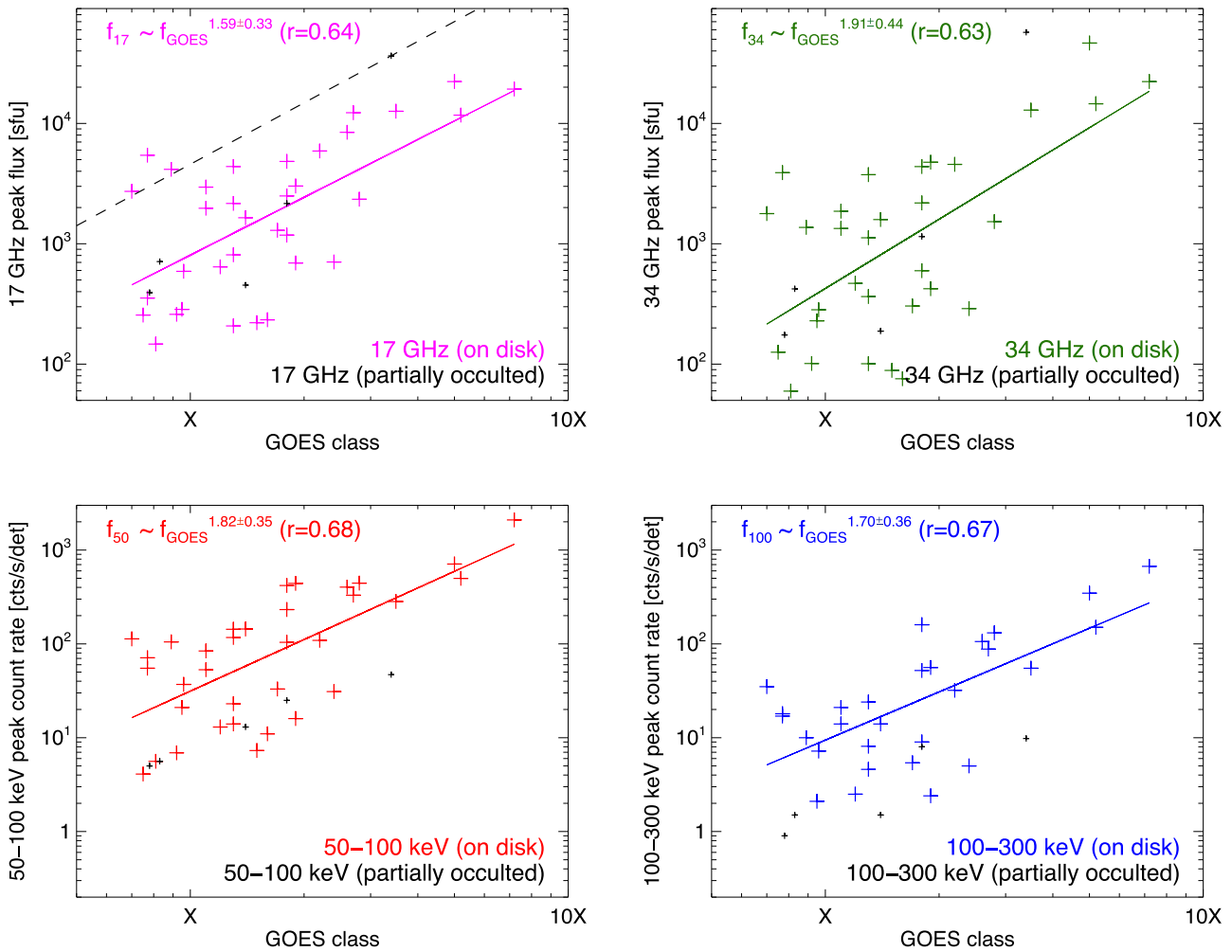
Figure 7. Scatter plots with GOES class: the top two plots show the correlation between GOES class and the NoRH peak flux, while the bottom plots compare the GOES class to the RHESSI peak count rates, as indicated. Partially occulted events are marked in black. The solid lines show power-law fits to the on-disk flares only, with the fit parameters shown in the top left corner of each plot. The black dashed line in the top left plot shows the correlation found if all flare sizes are included (Kawate et al. 2011). The correlation between the thermal GOES emission and the nonthermal emissions seen in radio and hard X-rays are moderate, with correlation coefficients around two-thirds.
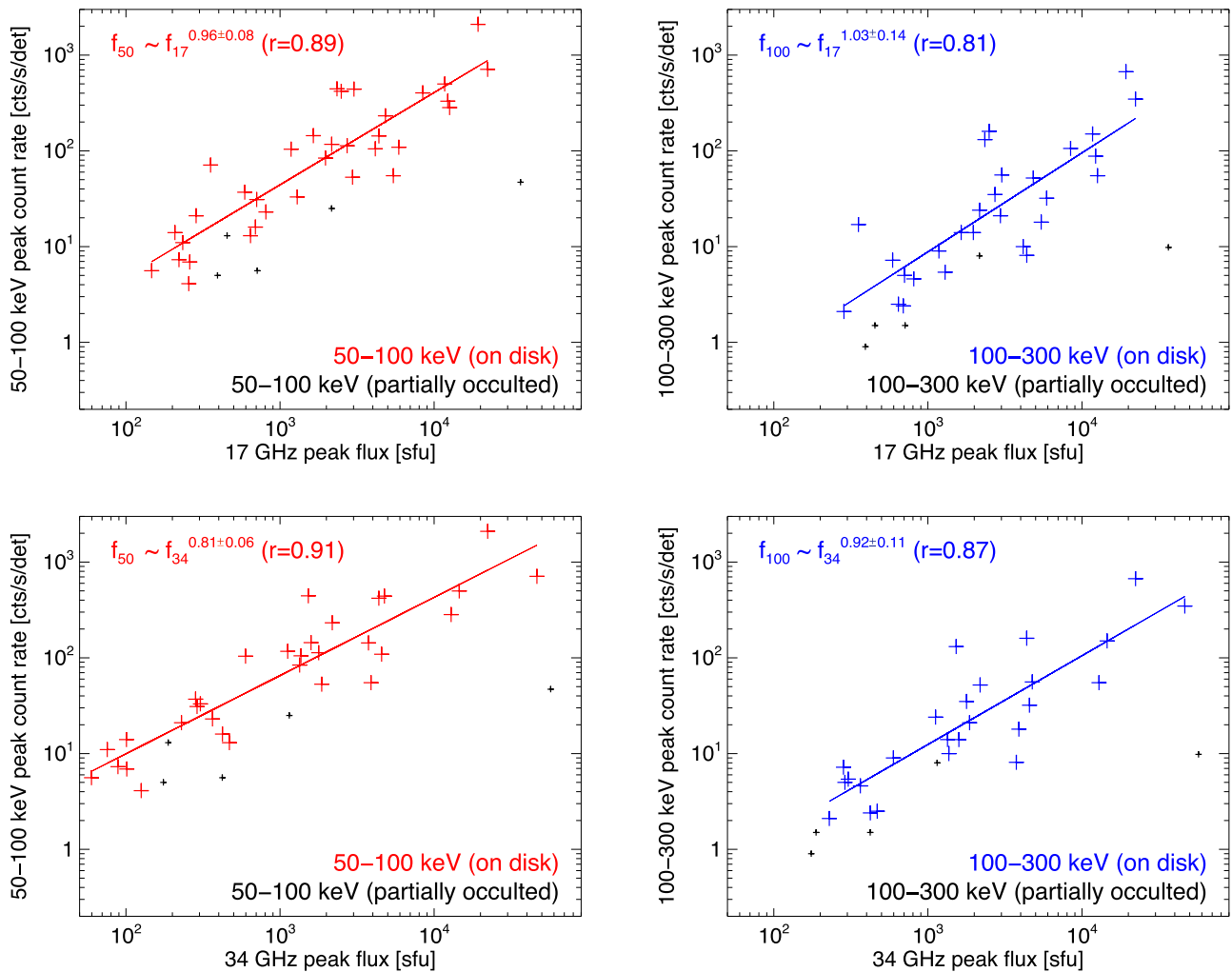
Figure 8. Scatter plots between the nonthermal peak fluxes seen in radio (17 and 34 GHz separately) and hard X-rays (50–100 keV and 100–300 keV separately), as indicated. Compared to correlation with the thermal peak fluxes, the two nonthermal quantities have a much better correlation coefficient and follow a nearly linear correlation.

nonthermal peak fluxes can be observed in flares whose peak soft X-ray emission differs by a factor of 500: a curious result in the context of the paradigm that the soft X-ray emitting plasma results from the precipitation of the electrons that produce the nonthermal hard X-rays.

2.2.2. Suzaku/WAM and NoRH Microflares

As mentioned above, the sensitivity limits of RHESSI and NoRP roughly match the correlation in the flare sample between the 50 and 100 keV count rates and the 17 GHz flux. To investigate even smaller events, we need to look for instruments with higher sensitivity. NoRH can detect fluxes down to about ∼0.1 sfu at 17 GHz, and it could therefore extend the correlation by almost 2 orders of magnitude. However, there is no hard X-ray instrument that matches such a sensitivity increase. During the time period relevant for our study, the most sensitive solar flare hard X-ray observations in the 50 keV range are provided by the WAM detector on the Japanese Suzaku satellite (Yamaoka et al. 2009). Ishikawa et al. (2013) published the jointly observed Suzaku/WAM-RHESSI microflares from solar cycle 23 (with GOES class at or below B level). The published Suzaku/WAM microflares are generally at or below the RHESSI 50 keV detection limit, but RHESSI detects these events clearly at lower

energies, typically between 10 and 50 keV. Through extrapolation of the RHESSI count spectrum, the expected RHESSI 50–100 keV count rates can be derived to allow us to extend our statistical study. Such an extrapolation is justified, as the Suzaku/WAM data clearly confirms that the emission extends up to 100 keV (see Figure 2 in Ishikawa et al. 2013). With Suzaku/WAM we therefore can increase the 50–100 keV sensitivity relative to RHESSI by about a factor of 5, allowing us to probe the radio/X-ray correlation toward smaller events. However, the much higher radio sensitivity may introduce a selection bias, with jointly detected flares tending to be hard-X-ray-rich.

Using the Suzaku/WAM flare catalog, we selected a total of 10 microflares of GOES class B or below that are jointly observed by Suzaku/WAM, RHESSI, and NoRH (see Figure 10 for two examples). Four of these events are from the original paper by Ishikawa et al. (2013), while six events are from the current solar cycle. Three additional WAM microflares were discarded as the extrapolations of the RHESSI data toward higher energies were questionable since Suzaku/WAM only detected these events up to 50 keV. The microflare data derived from Suzaku/WAM events are shown in black in Figure 9. The selection bias introduced by the hard X-ray detection limit of order 0.1 cts/s/det is consistent with the fact that most weak Suzaku/WAM events lie above the fitted line.
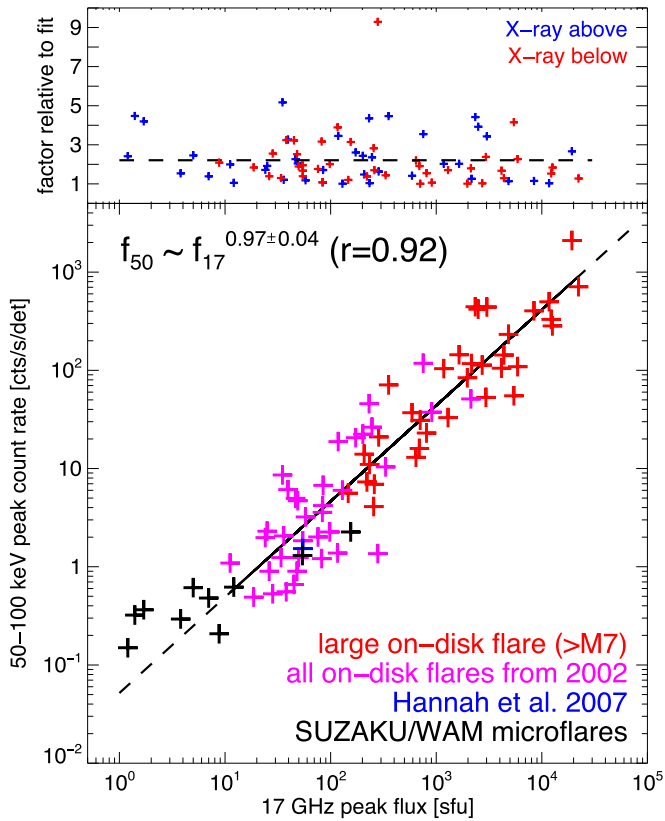
Figure 9. Correlation plot between the 17 GHz peak flux and the 50–100 keV peak count rate with smaller flares added. The top panel show the factor of deviation from the fit. In addition to the flares shown in Figure 5 (top right) smaller sized flares are added to extend the correlation.

Considering this bias, the additional data points are consistent with the correlation found at lower energies. This demonstrates that a linear correlation of bremsstrahlung and gyrosynchrotron emissions holds over at least 4 orders of magnitude.

2.3. Imaging at Radio Peak Time

For each of the 35 jointly observed NoRH/RHESSI flares we compared the radio and hard X-ray source morphology. For RHESSI imaging, we used the standard RHESSI CLEAN algorithm (Hurford et al. 2002) to make a 50–100 keV image for each flare by integrating over the main hard X-ray peak duration. This typically corresponds to an integration time between ~30 and ~100 s. As the nonthermal footpoints are generally compact, we used all RHESSI subcollimators for imaging. Depending on image morphology and counting statistics, we occasionally leave out the finest subcollimator to achieve a better image dynamic range. Additionally, we optimize the image dynamic range by using different subcollimator weighting schemes (i.e., "uniform" versus "natural"). Using all subcollimators, this results in images with FWHM resolutions of $3\rlap{.}''3$ ("uniform") and $5\rlap{.}''8$ ("natural"). For reference, we also made an image in the thermal range over the same time interval. As all selected flares are large flares, thermal emission extends up to high energies, and we use the energy range from 12 to 18 keV to represent the thermal emissions. As thermal sources are often extended compared to the angular scales of RHESSI's finest grids, we generally omit the two finest RHESSI subcollimators for imaging in the thermal range, which results in FWHM resolutions of $9\rlap{.}''8$ ("uniform") and $15\rlap{.}''5$ ("natural").

The Nobeyama Radio Heliograph data were converted to visibilities and processed in the AIPS package. Images were made at 1 s cadence for the entire duration of the flare, and deconvolved using the CLEAN algorithm for the bright emission. Thus the radio images correspond to shorter integrations than the hard X-ray images, but it is found that the radio morphology does not change significantly during the integration at the hard X-ray peak. The spatial resolution used to restore the resulting images is generally $12''$ at 17 GHz and $6''$ at 34 GHz. Since the dynamic range of the 17 GHz images near the flare peak is generally well over 10^3 for a 1 s image, it is possible to sacrifice some of the signal-to-noise and attain better spatial resolution in regions of the brightest emission, in a technique known as "super-resolution": we have used this technique in suitable cases to make 17 GHz maps with $6''$ resolution in order to better match the 34 GHz and RHESSI resolution.

After inspection of the sample of images at the hard X-ray peaks, our flare list can be divided into the following groups:

1. Extended: for 22 flares the spatial extent of the flare was large enough that we could clearly separate the chromospheric source locations and the associated radio sources. The hard X-ray images generally show two footpoints, in some cases slightly extended along the direction of the associated flare ribbons visible in chromospheric images, as is generally found in RHESSI flares (e.g., Dennis & Pernak 2009). The radio images show either emission from sources in both legs of the flaring loop that connects the hard X-ray footpoints, or from a single source peaking near the loop top. Within this group, we find the following distribution of source morphologies:
   (a) Leg/leg: six flares with the 17 and 34 GHz sources both from the leg of the flare loop.
   (b) Top/leg: six flares with the 34 GHz from the loop leg and 17 GHz from the loop top.
   (c) Top/top: 10 flares with the 17 and 34 GHz sources both from the loop top.

Figure 11 gives an example of each of these three event geometries.

2. Compact: for six flares the angular extent of the flare is small compared to the NoRH resolution, and no detailed source morphology could be established (see Figure 10, bottom right).
3. Unclear: for five events, the source morphology could not be established unambiguously.
4. Occulted flares: for two flares, the hard X-rays from the chromosphere are fully occulted, and we cannot study the source morphology. Note that the number of occulted events marked in Figures 7 and 8 is larger as it also includes events where the hard X-ray footpoints are visible, but whose fluxes are likely diminished by partial occultation.

In the next step we compare the peak fluxes of flares with the same source morphology to the correlation plot of the peak fluxes to search for systematic deviations. Figure 12 shows the selected data in each group relative to the correlation found for all flares (see Section 2.2). To simplify the discussions, we only show the correlation between 17 GHz and 50–100 keV, but the other correlations are similar. For flares with radio emissions from the legs of the loop at both frequencies, all data points are below the correlation curve. Hence, these events are radio rich, likely because the magnetic field strength is higher in the legs
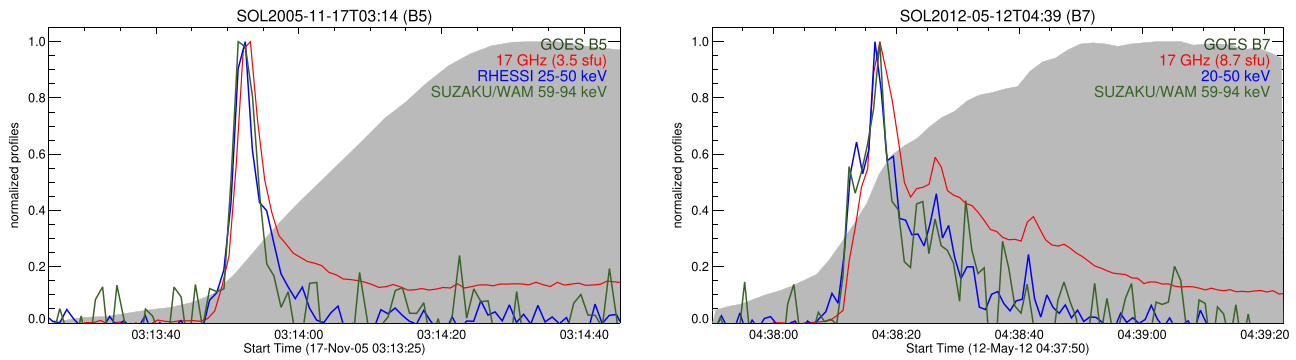
Figure 10. Time profiles of two of the smallest nonthermal flares included in this study that were simultaneously observed by NoRH, RHESSI, and Suzaku/WAM. The plots are in the same format as for the large flares shown in Figures 2 through 5. Despite their small size with fluxes at 17 GHz of only a few sfu, these tiny events show the same temporal behavior as large flares.
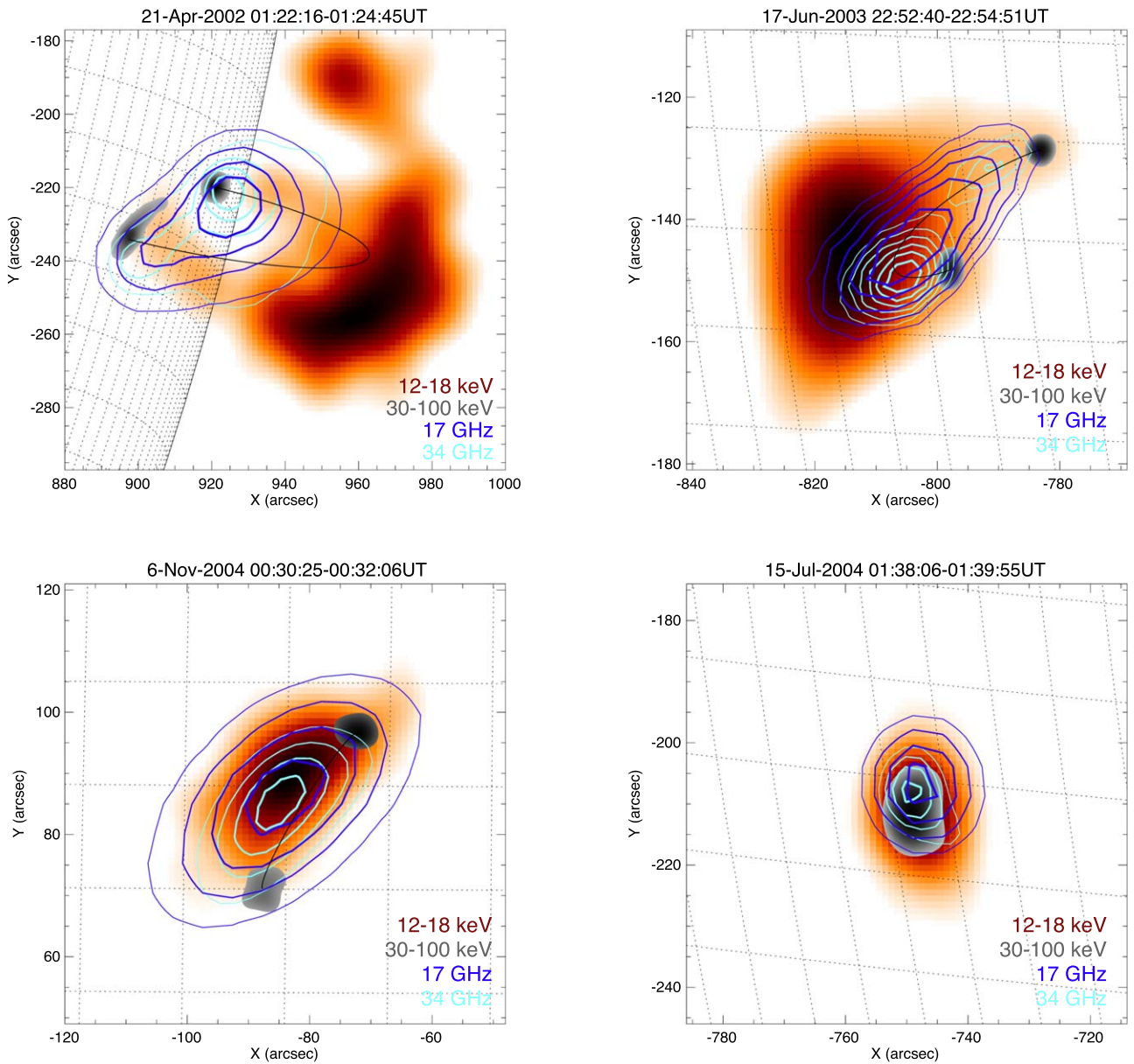
Figure 11. Imaging overview of four representative events from each morphological group: (top left) radio emissions at both NoRH wavelengths from the legs of the flare loop. (Top right) 34 GHz emission from the loop legs, while the lower frequency is most prominent from the loop top. (Bottom left) Both radio emissions from the loop top. (Bottom right) Compact sources.
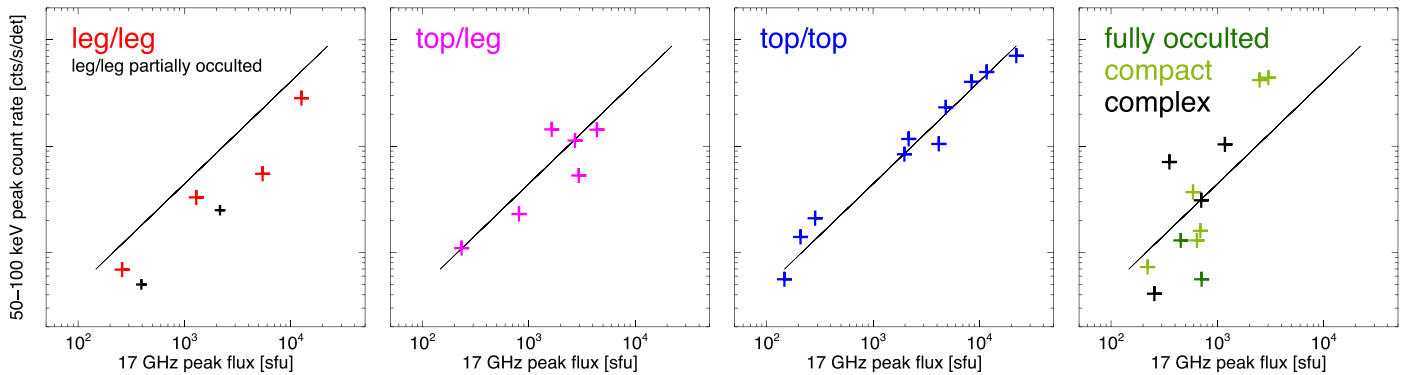
Figure 12. Comparing the overall peak flux correlation to flares grouped by different morphologies: Each separate plot corresponds to a different radio source morphology as indicated, see the text for details. For each plot, the correlation found in Figure 8 is shown as a black line for reference.

compared to the loop top. As two out of the six flares are at the limb (black points in Figure 12), we suspect that these two events exhibit somewhat lower hard X-ray emission because part of the hard X-ray ribbon might be hidden from Earth. Using only the four on-disk flares with emissions from the legs (red points in Figure 12), the averaged factor below the fit is 2.3 (with a standard deviation of 1.0). For events with only the 34 GHz emission originating from the flare legs, this effect is not clearly seen, but only one out of six flares is above the correlation curve. Flares with radio emissions from the loop top at both frequencies follow very closely the correlation found for the full sample. For these flares, the deviation from the fit is only a factor of around 1.3, compared to about 2 for all events, and the correlation coefficient is 0.985. For completeness we also show the correlation of the compact, fully occulted, and complex flares (together in the right panel in Figure 12), but no trend is obvious for these events.

3. Summary

We have initiated a statistical study of jointly observed NoRH/RHESSI solar flares observed during solar cycles 23 and 24. Our initial results for peak flux statistics strongly corroborate earlier findings with improved accuracy, but also provide new insights. The radio and hard X-ray peak fluxes during solar flares are found to be linearly correlated over four orders of magnitude, with individual events deviating on average by about a factor of two from the linear correlation. By combining peak flux and source morphology statistics, we further show that the correlation improves significantly when we compare flares with the same radio morphology. Such a restriction makes a more uniform selection of the magnetic field topology, and events with the same topology show an even closer correlation. Considering only flares with radio emission mainly from the top of the flare loop produces a much narrower correlation with less scatter, around a factor of 1.3. Similarly, restricting the flare list to events with radio emission from the legs of the flare loop, we find that these events are radio-rich by about a factor of ~2 relative to the linear correlation across the full sample.

These findings strongly support the idea that the same population of accelerated nonthermal electrons, or at least two very tightly correlated populations, produce both the gyrosynchrotron microwave emission and the bremsstrahlung hard X-ray emission in the impulsive phase of solar flares. Since it is much easier to produce such close correlations for higher magnetic field strengths (see Figure 1), the field strengths in the radio sources are more likely to be around 1000 G rather than 100 G, consistent with the fact that

flare radio spectra tend to peak at 10 GHz and above. The linear correlation of peak radio and hard X-ray fluxes over four orders of magnitude is in some ways surprising, since the optically thin radio flux depends so strongly on magnetic field strength ($\propto B^{3.4}$ for an electron power-law with $\delta = 4$) while the hard X-ray emissivity is essentially independent of B. The relative lack of spread in the quantitative relationship between nonthermal radio and hard X-ray fluxes would seem to indicate that the magnetic field strengths in nonthermal 17 GHz sources across a wide spectrum, from very small to very large flares, are likely quite similar.

These initial statistical results obtained by NoRH and RHESSI highlight the scientific value of these two data archives, and additional studies from the sample of large flares used here are underway. There remain many other features of solar flares that can be explored with these data sets, even as new radio facilities are becoming operational in the upcoming solar cycle 25.

ORCID iDs

Säm Krucker ⓘ https://orcid.org/0000-0002-2002-9180
Stephen M. White ⓘ https://orcid.org/0000-0002-8574-8629

References

Asai, A., Kiyohara, J., Takasaki, H., et al. 2013, ApJ, 763, 87
Bastian, T. S. 1999, in Proc. Nobeyama Symp., Solar Physics with Radio Observations, NRO Report No. 479, ed. T. Bastian, N. Gopalswamy, & K. Shibasaki (Kiyosato, Japan), 211

Benz, A. O. 2017, LRSP, 14, 2
Dennis, B. R., & Pernak, R. L. 2009, ApJ, 698, 2131
Dulk, G. A., & Marsh, K. A. 1982, ApJ, 259, 350
Hannah, I. G., Krucker, S., Hudson, H. S., Christe, S., & Lin, R. P. 2008, A&A, 481, L45
Hurford, G. J., Schmahl, E. J., Schwartz, R. A., et al. 2002, SoPh, 210, 61
Ishikawa, S., Krucker, S., Ohno, M., et al. 2013, ApJ, 765, 143
Kawate, T., Asai, A., & Ichimoto, K. 2011, PASJ, 63, 1251
Kawate, T., Nishizuka, N., Oi, A., et al. 2012, ApJ, 747, 131
Kosugi, T., Dennis, B. R., & Kai, K. 1988, ApJ, 324, 1118
Krucker, S., Battaglia, M., Cargill, P. J., et al. 2008, A&ARv, 16, 155
Krucker, S., Hudson, H. S., Glesener, L., et al. 2010, ApJ, 714, 1108
Krucker, S., & Lin, R. P. 2008, ApJ, 673, 1181
Kundu, M. R., Garaimov, V. I., White, S. M., et al. 2004, ApJ, 600, 1052
Kundu, M. R., White, S. M., Shibasaki, K., Sakurai, T., & Grechnev, V. V. 2001, ApJ, 547, 1090
Lin, R. P., Dennis, B. R., Hurford, G. J., et al. 2002, SoPh, 210, 3

Masuda, S., Kosugi, T., Hara, H., Tsuneta, S., & Ogawara, Y. 1994, Natur, 371, 495
Minoshima, T., Yokoyama, T., & Mitani, N. 2008, ApJ, 673, 598
Morgachev, A. S., Polyakov, V. E., & Melnikov, V. F. 2014, ARep, 58, 335
Nakajima, H., Nishio, M., Enome, S., et al. 1995, JApAS, 16, 437
Nakajima, H., Sekiguchi, H., Sawa, M., et al. 1985, PASJ, 37, 163
Peterson, L., & Winckler, J. R. 1958, PhRvL, 1, 205
Ramaty, R., Schwartz, R. A., Enome, S., et al. 1994, ApJ, 436, 941
Shih, A. Y., Lin, R. P., & Smith, D. M. 2009, ApJL, 698, L152
Silva, A. V. R., Wang, H., & Gary, D. E. 2000, ApJ, 545, 1116
Smith, D. M., Lin, R. P., Turin, P., et al. 2002, SoPh, 210, 33
Trottet, G., Vilmer, N., Barat, C., et al. 1998, A&A, 334, 1099
White, S. M., Benz, A. O., Christe, S., et al. 2011, SSRv, 159, 225
White, S. M., Krucker, S., Shibasaki, K., et al. 2003, ApJL, 595, L111
White, S. M., Kundu, M. R., Garaimov, V. I., Yokoyama, T., & Sato, J. 2002, ApJ, 576, 505
Yamaoka, K., Endo, A., Enoto, T., et al. 2009, PASJ, 61, S35